Hydrodynamics of a Compound Drop in Plane Poiseuille Flow

Vignesh Thammanna Gurumurthy[1, a)] and S. Pushpavanam[1, b)]
Department of Chemical Engineering, Indian Institute of Technology Madras, Chennai-600036, India

(Dated: 18 June 2020)

We numerically investigate the hydrodynamics of a two-dimensional compound drop in a plane Poiseuille flow under Stokes regime. A neutrally buoyant, initially concentric compound drop is released into a fully developed flow, where it migrates to its equilibrium position. Based on the results, we find that the core-shell interaction affects the dynamics of both the core and the compound drop. During the initial transient period, the core revolves about the center of the compound drop due to the internal circulation inside the shell. At equilibrium, depending upon the nature of the flow field inside the shell, we identify two distinct core behaviors: stable state and limit-cycle state. In the stable state, the core stops revolving and moves outward very slowly. The core in the limit-cycle state continues to revolve in a nearly fixed orbit with no further inward motion. The presence of core affects both deformation and migration dynamics of the compound drop. A comparison with the simple drop reveals that the core enhances the deformation of the compound drop. The outward moving core in stable state pushes the compound drop towards the walls, while the revolving core in limit-cycle state makes the compound drop to oscillate at its equilibrium position. The migration of the compound drop also affects the eccentricity of the core significantly. From the parametric study, we find that the core affects the compound drop dynamics only at intermediate sizes, and increase in any parameter sufficiently causes a transition from limit-cycle state to stable state.

arXiv:2004.06428v2 [physics.flu-dyn] 17 Jun 2020

I. INTRODUCTION

A compound drop, also called a double emulsion, is a multicomponent liquid system consisting of one or more drops encapsulated inside another immiscible drop. The outermost drop is often referred as the shell and the inner ones as the core. The shell functions as a protective layer to the core from the ambient fluid. This feature makes the compound drops to be used as a delivery system, where the core can be loaded with chemical reactants[1], drugs[2,3], and food additives[4]. In addition, it is also suited for in-situ culturing of cells and bacteria[3,5,6]. Thus compound drops are highly desirable for applications related to bioanalysis, cosmetics, food and pharmaceutical industries.

Majority of the fundamental works on compound drops have focussed primarily on their production techniques and their dynamics in three basic flow geometries: (i) translation in a quiescent liquid[7–10], dynamics in (ii) extensional flows[11–13] and (iii) linear shear flows[11,14–19]. But, the pressure-driven flow (also known as Poiseuille flow) often encountered in microfluidic and biological systems has not been examined thoroughly yet. The stability of the compound drops moving in these flows play a huge role in applications related to targeted release of active ingredients in the core[2]. Thus, understanding the dynamics of compound drops in Poiseuille flow is crucial for the aforementioned applications.

Very few studies have investigated the dynamics of compound drops in Poiseuille flow[20–24], but they are not applicable at all conditions due to their underlying assumptions. The theoretical work by Song *et al.*[21] studied the dynamics under Stokes regime in a capillary tube assuming both the shell and the core are perfectly spherical. Their analysis shows that the drag force on the core and the shell depends on various parameters such as the viscosity ratio between the liquids (core-shell, shell-carrier), size ratio between the core and the shell, and eccentricity of the core. The use of perfectly spherical drop assumption limits their applicability since it is well known that the drops deform due to the confinement effects[25] which alters its shape. The numerical works by Zhou *et.al*[20] and Tau *et.al*[22] investigated the morphological evolution of the compound drop moving in circular tube with a gradual contraction using phase field and boundary element methods, respectively. Both studies show that the core affects the deformation of the compound drop and also prolongs the transit time in the contraction zone. Studies by Che *et.al*[24] and Borthakur *et.al*[23] simulated the dynamics of compound drop in circular microchannels under axisymmetric conditions using level-set and volume-of-fluid methods respectively. They investigated the temporal evolution of the drop shape, velocity fields, and the eccentricity of the core under the influence of parameters such as size of the compound drop, radius ratio, viscosity ratio and the capillary number.

The use of axisymmetry in the above studies limits their results to compound drops moving in circular microchannels. In addition, the axially moving drops (core and shell) are always at the centerline of the channel due to axisymmetry. But we know from theory of migration for simple drops[26], that only large drops comparable to channel size occupies the center, whereas smaller drops often migrate to an off-centered position. Recent experiments[27] have shown that the migration of compound drops in flow focusing geometries experience enhanced deformation. Thus, the effect of migration of the compound drop on the core, and the effect of core on the migration of the compound drop has not yet been understood clearly, and this forms the primary focus of this work.

In this work, we investigate the dynamics of the compound drop in a plane Poiseuille flow, which includes the migration and deformation dynamics of the core and the compound

a)Electronic mail: vigneshtg@gmail.com
b)Electronic mail: spush@iitm.ac.in

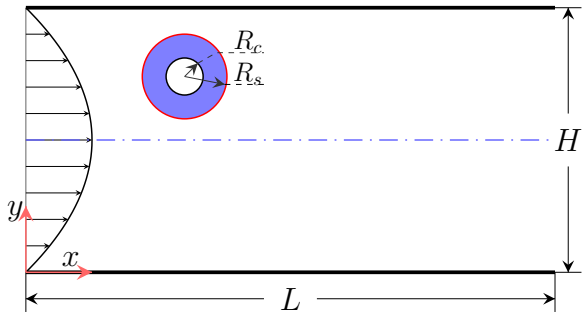

FIG. 1: Schematic of the computational domain. A neutrally buoyant, initially concentric compound drop is released into the fully developed flow.

drop. The objectives of this study are to understand the (i) effect of migration of the compound drop on the dynamics of the core, (ii) effect of core on the migration and deformation of the compound drop, and (iii) analyze their dynamics under the influence of different parameters involved.

Rest of the paper is organized as follows. In section II, we define the problem, list the governing equations and describe the numerical method adopted. In section III, we first describe the dynamics of the core followed by the compound drop, and finally the influence of different parameters on the equilibrium behaviors of the core and the compound drop. Finally, we summarize the results in section IV.

II. PROBLEM FORMULATION

A. Problem definition

Consider a concentric compound drop released in a fully developed plane Poiseuille flow as shown in Fig. 1. We choose the subscripts c, s, and d to denote the parameters related to the core, shell and the compound drop, respectively. The radius of the undeformed core and shell are denoted as R_c and R_s, respectively. We choose the commonly used core-shell-carrier fluid configuration in experiments: water-in-oil-in-water (W/O/W). This choice simplifies our problem to a two-phase flow since the core and the carrier phase are of the same liquid. The liquids are assumed to be Newtonian, and neutrally buoyant.

B. Governing equations

We model the two-phase flow using Volume-of-Fluid (VOF) method, where a single set of governing equations describe the flow in the domain occupied by the two phases. The two phases are treated together as a continuum with variable material properties which abruptly changes at the interface. Since the flow rates associated with the microfluidic systems are typically low, Stokes flow conditions are assumed. The governing equations are,

$$\nabla \cdot \mathbf{U} = 0, \tag{1}$$

$$-\nabla P + \nabla \cdot (\mu \mathbf{D}) + \sigma \kappa \mathbf{n} \delta_s + \mathbf{S_p} = 0, \tag{2}$$

where μ, $\mathbf{U}$ and P represent viscosity, velocity and pressure field, respectively. The rate of strain tensor $\mathbf{D}$ is defined as $(\nabla \mathbf{U} + \nabla \mathbf{U}^T)$. The third term on the right hand side of Eq. (2) represents the surface tension force acting at the interface modelled as a body force term according to continuum surface force formulation[28]. The use of Dirac delta function δ_s ensures that this force acts only in the vicinity of the interface and zero anywhere; Also, it acts along the direction of the normal $\mathbf{n}$ to the interface. The symbols σ and κ denote the surface tension coefficient and curvature of the interface, respectively. The flow through the channel is driven by a constant pressure gradient which is introduced as a source term $\mathbf{S_p}$ in Eq. (2) (see appendix A for derivation). It is given by,

$$\mathbf{S_p} = \frac{8\mu_c U_m}{H^2}\hat{\mathbf{x}},$$

where U_m is the maximum velocity observed at the centerline of the channel in the absence of the drop, and H is the channel height.

The two phases are distinguished by the scalar field f, which represents the volume fraction of the shell liquid. Computational cells with $f = 1$ represent the shell phase and $f = 0$ represent either the core or the carrier phase. Thus cells with f values between zero and one contain the interface whose motion is governed by the advection equation,

$$\frac{\partial f}{\partial t} + \nabla \cdot (f\mathbf{U}) = 0. \tag{3}$$

The viscosity is now defined as,

$$\mu = \mu_s f + (1-f)\mu_c. \tag{4}$$

C. Non-dimensionalization

We non-dimensionalize the above equations (1)-(4) using the channel height H, centerline velocity U_m, and the ratio $\tau = H/U_m$ as the characteristic length, velocity, and time scale, respectively. The characteristic time τ scale used here is the time required for advecting the volume fraction field i.e, interface. Pressure is scaled using the viscous friction given by $\mu_c U_m/H$, and the viscosity in Eq. (4) using μ_c. We write the non-dimensionalized equations in the same form as their dimensional counterparts for convenience, and they are given below,

$$\nabla \cdot \mathbf{U} = 0, \tag{5a}$$

$$-\nabla P + \nabla \cdot (\mu \mathbf{D}) + \frac{\kappa \mathbf{n} \delta_s}{Ca} + 8\hat{\mathbf{x}} = 0, \tag{5b}$$

$$\frac{\partial f}{\partial t} + \nabla \cdot (f\mathbf{U}) = 0, \tag{5c}$$

and the viscosity is given by,

$$\mu = \mu_r f + (1 - f). \tag{5d}$$

In Eq. (5b), $Ca = \mu_c U_m/\sigma$, represents the capillary number which is the ratio between viscous and capillary forces, and $\mu_r = \mu_s/\mu_c$ in Eq. (5d) represents the viscosity ratio between the two liquids. In addition, the dynamics of the compound drop also depends on the radius ratio $K = R_c/R_s$, and aspect ratio $\lambda = R_s/H$. The radius ratio signifies the confinement effects of the shell on the core, while the aspect ratio signifies the confinement effects the wall.

D. Numerical method

We solve the quasisteady Stokes equations using pseudo-transient method. In this method, by including the unsteady acceleration term in Eq. (5b) we construct an unsteady equation as shown below,

$$\frac{\partial \mathbf{U}}{\partial t} = -\nabla P + \nabla \cdot (\mu \mathbf{D}) + \frac{\kappa \mathbf{n} \delta_s}{Ca} + 8\hat{\mathbf{x}}. \tag{6}$$

The transient solution of the above unsteady equation is marched in time until steady state is reached.

The governing equations are solved numerically using the open source code Basilisk[29,30] written in C programming language. The equations are discretized using finite volume method where the primitive variables (u, v, P, f) are collocated at the cell centers. The discretizations are second-order accurate in both space and time. Equations (5a) and (6) are solved using a pressure projection approach, and the advection equation (5c) using an operator-split algorithm. The surface tension force in Eq. (6) is accurately calculated using balanced force algorithm[31], and the curvature of the interface is computed from the volume fraction field using height functions technique[30,32].

Basilisk provides an adaptive mesh refinement technique, which is used for refining specific regions to improve accuracy. The refinement is based on a wavelet transform of a given scalar field, which is used to assess its discretization error. The grid is locally refined if the calculated error is above the user-specified threshold and coarsened otherwise. In the simulations presented here, the threshold values are fixed at 1×10^{-3} and 1×10^{-2} for the two velocity components (u, v) and the volume fraction field (f), respectively. These values ensure that the regions close to the interfaces are sufficiently resolved for accurate calculation of the surface tension force.

Due to the explicit treatment of surface tension force in basilisk, the time step is calculated according to the Brackbill criterion[28],

$$\Delta t \leq \sqrt{\frac{\rho \Delta x^3}{\pi \sigma}} \tag{7}$$

which is the time step required to resolve the propagation of shortest capillary wave resolved by the mesh. By comparing equations (2) and (6) the above condition reduces to,

$$\Delta t \leq \sqrt{\frac{\Delta x^3 Ca}{\pi}}. \tag{8}$$

The above equation shows that the time step is directly proportional to the capillary number i.e., deformation.

E. Computational domain and boundary conditions

As often reported in the literature[33–35], simulating cross stream migration of a drop is time consuming because the rate of migration is inversely proportional to the deformation of the drop. In addition, the time steps given by Eq. (8) decreases with the decrease in Ca. Thus, it takes longer time for the drop to reach its equilibrium location. Hence, we restrict our investigations to two dimensions. Nevertheless, previous works[33,34] have shown that the 2D simulations qualitatively captures the flow field obtained in the center plane of 3D simulations. Also, there is a good quantitative agreement for the equilibrium position of the drop calculated between the 2D simulations and the experiments[33,34].

The computational domain, as shown in Fig. 1, is a rectangular domain of size $L \times H$. No slip and no penetration boundary conditions are enforced at the top and bottom walls, and a periodic boundary condition in the horizontal direction. The size of the computational domain is chosen as 2×1 for smaller drops ($\lambda \leq 0.2$) and 4×1 for larger drops. These different domain lengths for different drop sizes are chosen such that the drop-drop interaction due to periodicity is negligible.

As mentioned above, since the migration of a drop to its equilibrium position is time consuming, it is advisable to release the drops closer to its equilibrium position. However, the equilibrium positions are not known a priori. Based on the literature on migration of simple drops[26,33,34], and from few trial and error simulations, we adopt the following approach. For simulations with $Ca < 0.25$ we release the concentric drop at $y_i = 0.65$ and at $y_i = 0.6$ for $Ca \geq 0.5$.

We characterize the dynamics of the compound drop, and the core by studying their migration and deformation behavior. The migration of the compound drop is characterized by its height y_d measured from the bottom wall. In case of the core, we report its eccentricity which is defined as $\vec{\varepsilon} = \vec{x_c} - \vec{x_d}$ (see Fig. 2(a)), where $\vec{x_c}$, $\vec{x_d}$ are the centroids of the core and the compound drop, respectively. The deformation characteristics of the core and the compound drop are quantified by calculating the deformation parameter $\mathscr{D}$ proposed by Taylor[36], which is defined as $\mathscr{D} = (\mathscr{L} - \mathscr{B})/(\mathscr{L} + \mathscr{B})$. Here, $\mathscr{L}$ and $\mathscr{B}$ denote the length of the major and minor axis of the deformed droplet as shown in Fig. 2(b). Each simulation is stopped shortly after equilibrium is reached i.e, when the parameters measured either attain a constant value or enter a periodic state.

Based on grid convergence tests (see appendix B), the size of the smallest region resolved in our simulations is 1.95×10^{-3}. We also have validated the code with the experiments

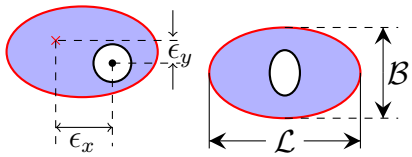

(a) (b)

FIG. 2: Schematics showing the definition of (a) the eccentricity of the core and (b) the deformation of the compound drop. The black dot and the red cross markers in (2a) represent the centroid of the core and the compound drop, respectively.

and the simulations reported in the literature on simple drops released in pressure-driven flows (see appendix C).

III. RESULTS AND DISCUSSIONS

A. Dynamics of the core

In this section, we describe the characteristics of two distinct core behaviors commonly observed in the simulations, and also explain its cause by analysing the flow field inside the shell.

1. *Distinct core behaviors*

The temporal evolution of the eccentricity of the core is shown in Fig. 3(a) and Fig. 3(b) under two different conditions: (i) $Ca = 1$ and (ii) $Ca = 0.05$. The other parameters were kept fixed at $\lambda = 0.2$ and $K = 0.5$, for both the cases. Initially, under both conditions, we observe oscillations in the eccentricity in both directions. Eventhough they are slightly out of phase with each other, their magnitudes are nearly the same. In the first case, the oscillations decay at a faster rate, eventually reaching a constant value. We call this equilibrium behavior as stable state. The oscillations in the second case decay slightly and enters a periodic state at long-times where it continues to oscillate at constant amplitude. We refer this periodic behavior as limit-cycle state. Thus at equilibrium, we observe two distinct behaviors, which have also been observed for compound drops in linear shear flows[17,18,37].

The oscillations of the core observed in both directions indicate that it revolves inside the shell around the centroid of the compound drop, as illustrated in Fig. 3(c) and Fig. 3(d). The core, as it revolves also moves inward in both cases. This revolving motion is due to the internal circulation inside the shell[38], which is the result of shearing of the shell interface due to the difference in velocities between the interface and the carrier fluid. The anticlockwise direction of both the circulation (see Fig. 4(b) & Fig. 4(d)) and the revolving motion of the core confirms that the core revolves due to the circulation.

In the stable state, as the core revolves, the length of its orbit reduces rapidly in each cycle in the same fashion similar to the decay of oscillations observed in Fig. 3(a). As shown in the inset in Fig. 3(c), at equilibrium, the core stops revolving and starts translating outwards. The velocity of the core in this outward motion can be inferred from the small distance travelled to be very small. The core in the limit-cycle state, also starts revolving and moving inward initially. But at equilibrium, it enters into an egg shaped orbit (see Fig. 2(d)), where its length in each cycle remains nearly the same thereafter, and also, it does not move inward any further.

2. *Underlying mechanism*

The two distinct core behaviors at equilibrium can be explained by analysing the rotational flow field they experience inside the shell. The gradient of the velocity field in any incompressible flow can be decomposed into strain rate tensor and vorticity tensor. The former causes deformation, while the latter causes rigid body rotation. A drop in pure straining field will undergo planar extension: stretching and compressing the drop along the principal axes. In a pure vorticity field, a drop while retaining its initial (spherical) shape will undergo rigid body rotation and align itself along the symmetry axis[39]. In a linear shear flow, where these two components are in equal proportion, the drop would stretch linearly in time and tilt toward the flow direction[40].

In the Poiseuille flow simulated here, we identify the magnitude of strain rate tensor from the deformation of the core, and the vorticity tensor from the local vorticity field. From Fig. 4(b) and Fig. 4(d), we see that the magnitude of the vorticity field in limit-cycle state is higher than in the stable state. The prolate ellipsoid and the circular shapes of the core in Fig. 4(b) and Fig. 4(d) clearly show that the deformation is higher in the stable state. This qualitative conclusion is further supported by the quantitative measurements of the deformation shown in Table I, where we observe that the deformation parameter $\mathscr{D}$ for the core in stable state is one order of magnitude higher than the limit-cycle state. Thus, large deformation and small vorticity field experienced by the core in stable state shows that the strain rate tensor is dominant. This dominant strain rate tensor aligns the core along the principal axes (see Fig. 4(b)) thereby arresting its revolving motion. The dominant vorticity field in the limit-cycle state causes the core to revolve in a nearly fixed orbit which resembles rigid-body rotation. It also causes the extensional axis of the core along which it is stretched, to oscillate as shown in Fig. 5.

3. *Deformation dynamics*

As the core revolves, it comes closer to the shell interface in each cycle. At this instant, the liquid in the gap between the two interfaces gets squeezed causing a pressure buildup which affects the deformation of the core every time it comes near the shell interface. This pressure buildup decreases in each cycle as the core moves inward due to increase in the thickness of the gap. Thus, the deformation of the core characterized by the deformation parameter $\mathscr{D}$ oscillates as seen

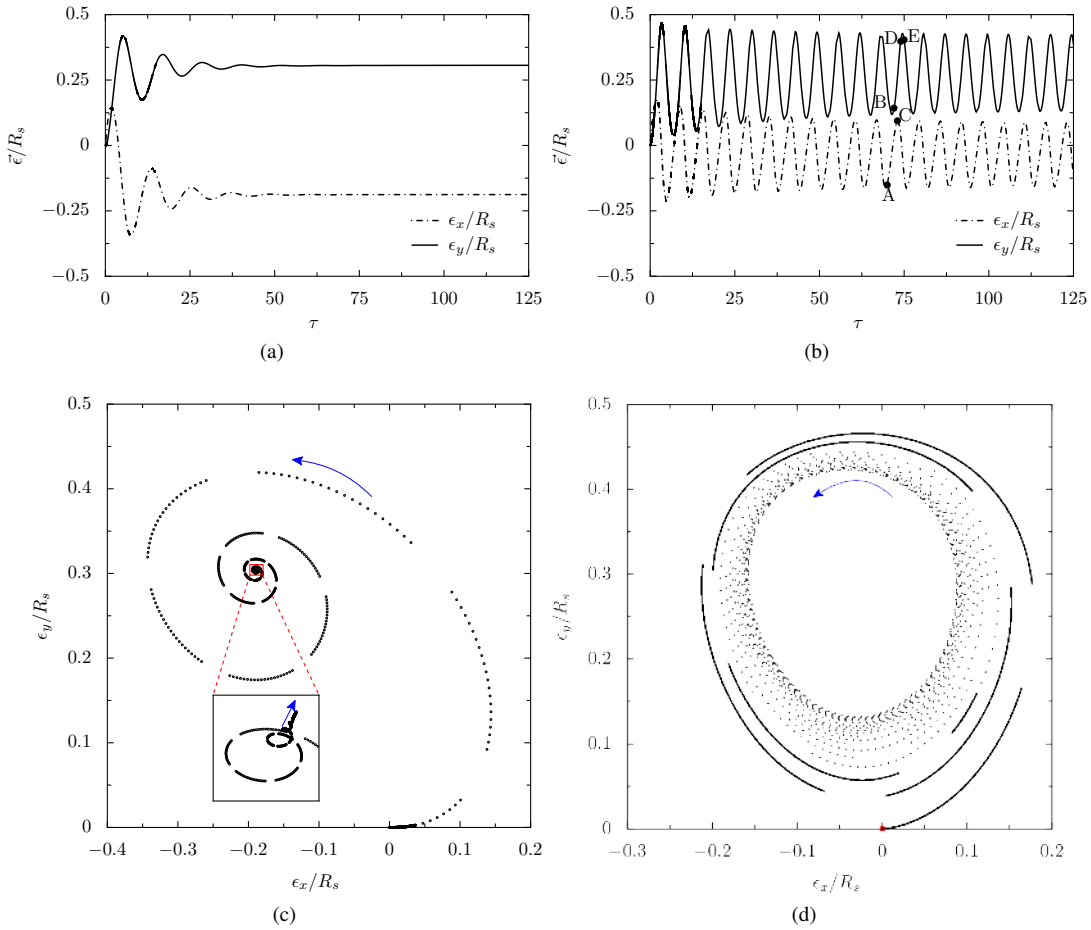

FIG. 3: Temporal evolution of the eccentricity of the core under (a) stable state and (b) limit-cycle state. Trajectory of the core inside the shell under (c) stable state and (d) limit-cycle state. The gaps seen in the trajectory of the core are due to the data ignored because of periodic boundary conditions. The eccentricity and the trajectory of the core are measured relative to the centroid of the compound drop ($\vec{\varepsilon} = \vec{x}_c - \vec{x}_d$). The common parameters between the two states are $\lambda = 0.2$, $K = 0.5$, $\mu_r = 1$ and the capillary number was kept fixed at $Ca = 1$ for the stable state and $Ca = 0.05$ for the limit-cycle state.

in Fig. 6(a) and Fig. 6(b). These oscillations in the case of a stable state decay with time, and reaches a constant value once the core stops revolving. The deformation of the core in the limit-cycle state continues to oscillate due to its revolving motion. The kinks (point D in Fig. 6(b)) observed in $\mathscr{D}$ at each cycle are due to the slightly out of phase nature of the oscillations of the core. As shown in Fig. 5(d) and Fig 5(e), the core reaches its maximum displacement in both directions one after the other which in turn affect their deformation thereby resulting in the kinks. Similar trends have also been reported in temporal evolution of the deformation of the simple drop in Poiseuille flow under Stokes conditions[41].

B. Dynamics of the compound drop

1. *Deformation*

The temporal evolution of the deformation parameter $\mathscr{D}$ of the compound drop in the two states are shown in Fig. 6(a) and Fig. 6(b). In each state, the oscillations in $\mathscr{D}$ for the compound drop is very similar to the ones in the core. Similar oscillations in $\mathscr{D}$ have also been observed for compound drops in linear shear flows[17,18,37]. These oscillations are due to the revolving motion of the core. Thus the parameter $\mathscr{D}$ attains a constant value in the stable state once the core stops revolving, whereas it continues to oscillate in the limit-cycle state like the core. As expected, the deformation of the compound drop in the stable state is significantly larger than in the limit-cycle state since Ca is larger for the stable state. The deformation of the compound drop in both states is larger than the core which is expected since the capillary force is inversely proportional to the drop size.

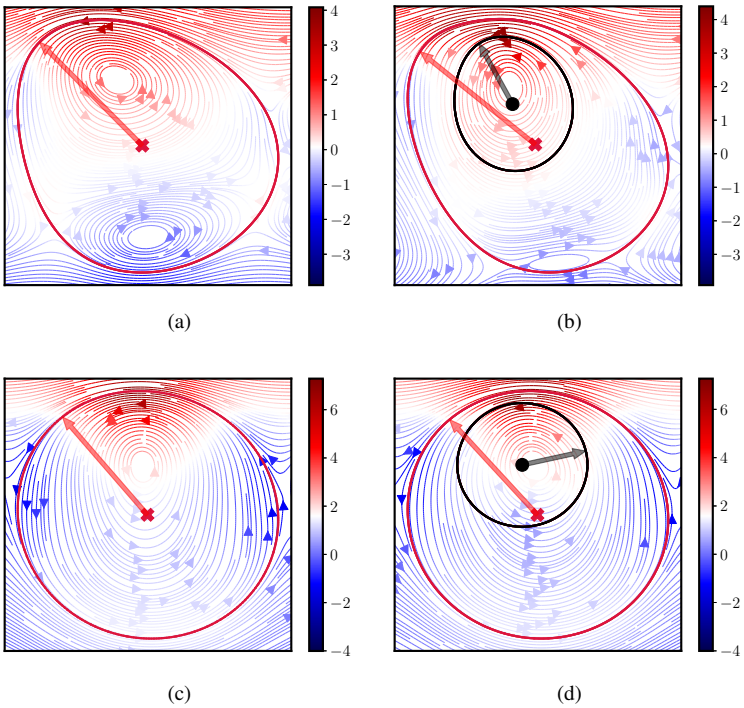

FIG. 4: Comparison of streamlines between simple drop and compound drop at equilibrium: (a) simple drop (b) compound drop in stable state (c) simple drop (d) compound drop in limit-cycle state. The streamlines are colored by the vorticity whose magnitude is given by the colorbar. The red cross marker represents the centroid of the compound drop, and the red arrow represents the extensional axis of the compound drop along which the it experiences maximum deformation. Similarly, the black dot and the black arrow represent the centroid and the extensional axis of the core, respectively. The parameters used are the same as shown in Fig. 3.

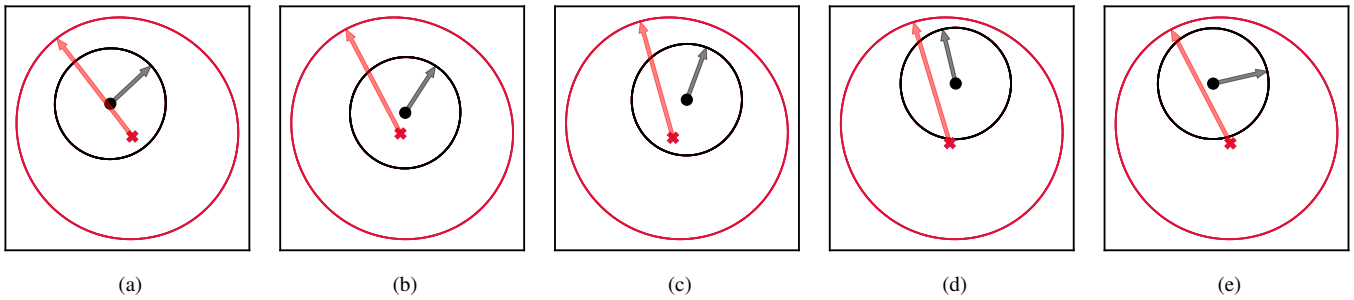

FIG. 5: Revolving motion of the core in limit-cycle state. Figures (a)-(e) represent the position of the core inside the shell at points *A*-*E* in Fig. 3(b). The red cross marker and the black dot represent the centroids of the compound drop and the core, respectively. The arrows in red and black colours represent the extensional axis of the compound drop and the core, respectively.

λ	K	μ_r	Ca	Core			Compound		Simple	
				ε_x	ε_y	$\mathscr{D}$	y_d	$\mathscr{D}$	y_d	$\mathscr{D}$
0.2	0.5	1	0.05	0.035±0.124	0.278±0.145	0.004±0.003	0.672 ± 0.002	0.026±0.002	0.681	0.026
0.2	0.5	1	1	-0.188	0.307	0.061	0.572	0.165	0.537	0.128

TABLE I: Equilibrium characteristics of the core and the compound drop in stable state ($Ca = 1$) and limit-cycle state ($Ca = 0.05$). The equilibrium behavior of the compound drop is also compared with the simple drop under the same conditions.

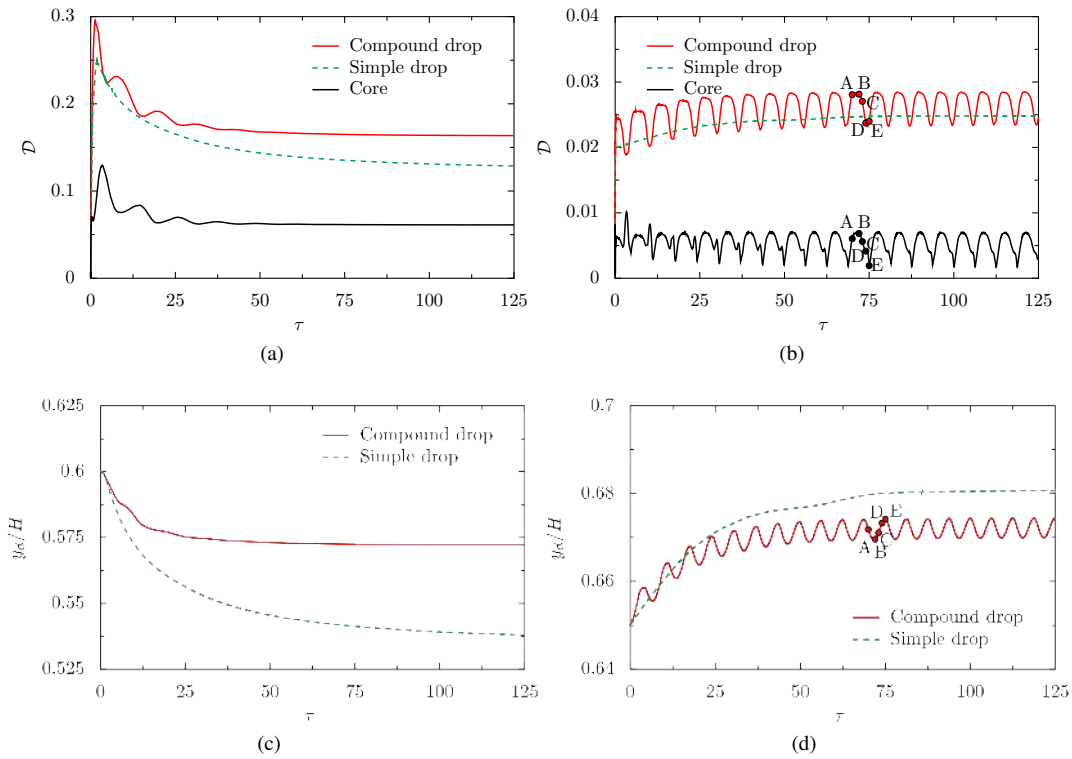

FIG. 6: Temporal evolution of the deformation parameter $\mathscr{D}$ of the compound drop and the core under (a) stable state and (b) limit-cycle state. Temporal evolution of the trajectory of the compound drop under (c) stable state and (d) limit-cycle state. The trajectory and the deformation of the compound drop are also compared with the simple drop under the same conditions. The parameters used for the two states were the same as in the Fig. 3.

As explained in the previous section, there is a pressure buildup in the gap between the core and the shell in each cycle when the core comes closest to the shell. This pressure buildup results in stretching of the shell which then relaxes as the core moves away from the shell. This cycle of stretching and relaxing of the shell resembles breathing, which has also been reported for compound drops in linear shear flows[17,18]. This breathing motion is very prominent in the stable state during the initial stages as the deformation of the compound drop is higher than in the limit-cycle state (see Fig. 1 and Fig. 2 in the supplementary information). This cycle of stretching and relaxing of the compound drop is reflected as oscillations in $\mathscr{D}$ shown in Fig. 6(a) and Fig. 6(b). By comparing the core positions $(A-E)$ in Fig. 5 with the corresponding $\mathscr{D}$ values in Fig. 6(b), we find that the deformation of the compound drop increases when the core is further away from the shell interface, and decreases when the core is closer to the interface.

The effect of core on the compound drop is evaluated by comparing the temporal evolution of $\mathscr{D}$ with the simple drop (see Fig. 6(a) and Fig. 6(b)). The deformation of the compound drop in the stable state is slightly larger than the simple drop. In the limit-cycle state where $\mathscr{D}$ continues to oscillate, the maximum $\mathscr{D}$ observed in each cycle is higher than the simple drop, while its minimum is lower than the simple drop. In addition to enhancing $\mathscr{D}$, the presence of core also alters the shape of the compound drop when compared to the simple drop. The parachute shaped simple drop transforms to an egg shape due to the core in stable state (see Fig. 4(a) and Fig. 4(b)). Both the compound drop in the limit-cycle state and the simple drop retain their initial circular shape due to low deformation. The extensional axis of the drop along which the drop is stretched for both simple and compound drop in stable state are in the same direction. As show in Fig. 5, the extensional axis of the compound drop in limit-cycle state oscillates due to the revolving core. Thus from the above comparison with the simple drop, we find that the presence of core enhances the deformation of the compound drop.

2. *Migration*

In a non-inertial flow, the cross stream migration of a simple drop occurs due to its deformation. This deformation might be due to either the hydrodynamics of the flow or the confinement effects from the wall or a combination of both. The deformation induced lift force always pushes the drop towards the center of the channel where the deformation is minimum[33–35], and its magnitude is proportional to the deformation. The drop also migrates towards the wall if $1 \leq \mu_r < 10$[26,42]. The above results apply only to small drops ($\lambda < 0.3$); larger drops ($\lambda \geq 0.3$) always occupy the center due to confinement effects.

We quantify the migration of the compound drop by measuring its height y_d from the bottom wall. The temporal evolution of migration of the compound drop and the simple drop are shown in Fig. 6(c) and Fig. 6(d) for both the states. The direction of migration of the compound drop is the same as the simple drop in both states. When compared to a simple drop, the compound drop oscillates during its migration. These oscillations are markedly noticeable in the limit-cycle state and continues to do so even after reaching equilibrium. In the stable state, we observe only minor undulations during its migration which stops once it reaches its equilibrium position. By comparing the core positions marked by the points B, D, E in Fig. 3(b) with the corresponding location of the drop in Fig. 6(d), we see that they reach their maximum and minimum heights together in each cycle. This synchronized motion is a result of the core pushing the shell upward as it reaches its peak in each cycle. Similar oscillatory motion due to the core has been observed experimentally in self propelling encapsulated nematic shells[43].

The equilibrium position of the compound drop is slightly higher than the simple drop in the stable state whereas it is slightly lower than the simple drop in the limit-cycle state. The slow upward motion of the core after it stops revolving in the stable state pushes the compound drop outward resulting in its slightly higher equilibrium position. The compound drop in the limit-cycle state is closer to the centerline than the simple drop. This is due to the slightly larger deformation induced lift force for the compound drop from its maximum deformation in each cycle, which is larger than the deformation of the simple drop (see Fig. 6(b)). The continued revolving motion of the core in the limit-cycle state also makes the compound drop to oscillate at its equilibrium position. Thus, the presence of core affects the migration of the compound drop.

The change in the equilibrium position of the compound drop due to the core also affects the circulation pattern inside the shell. We know that the circulation is the result of shearing of the shell interface due to the difference in velocities between the interface and the surrounding fluid. This shearing changes with position of the drop since the fluid velocity changes with the position. From Fig. 4(a) and Fig. 4(b), we observe that the circulation in the bottom half of the simple drop reduces significantly in the compound drop due to its slightly higher position. Since the compound drop in the limit-cycle state and its equivalent simple drop are completely in the upper-half of the channel, we observe from Fig. 4(c) and Fig. 4(d) only a slight shift in the center of the circulation. At equilibrium, when the core has stopped revolving in stable state, it migrates to the center of the circulation region.

By altering the circulation inside the shell, the migration of the compound drop also influences the position of the core i.e., eccentricity. When there are multiple circulation regions inside the shell, the core is always driven by the circulation dominant in size and magnitude. Thus, when the compound drop is off-centered, the core occupies an asymmetric position. Different core configurations due to the migration of the compound drop are shown in Fig. 7. The parameters used for the different configurations and the corresponding equilibrium positions are listed in the Table II. The eccentric

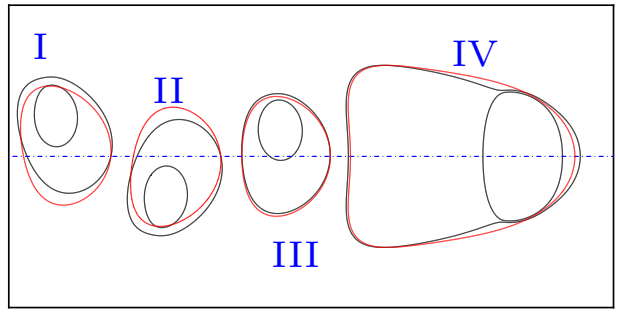

FIG. 7: Effect of migration of the compound drop on the eccentricity of the core. The interface shapes shown in red and black colours represent the simple and compound drops, respectively. The blue dash-dotted line represents the centerline of the channel. The parameters used for these cases are given in the Table II.

Index	λ	K	μ_r	Ca	y_{eq}/H	
					Simple	Compound
I	0.2	0.5	1	1	0.537	0.572[1]
II	0.2	0.5	1	1	0.464	0.427[1]
III	0.2	0.5	0.1	1	0.5	0.509
IV	0.4	0.5	1	1	0.5	0.5

[1] Initial release heights for drops I and II are 0.6 and 0.4, respectively.

TABLE II: Parameters used for cases shown in Fig. 7.

positions of the core shown in Fig. 7 are often observed in experiments[5,38,44,45]. It is well known that for a drop moving in a channel (2D) two equilibrium locations exists on either side of the centerline. From drops *I* and *II* in Fig. 7 we find that the position of the core switches to opposite sides depending upon the equilibrium position of the compound drop (either in top or bottom half of the channel). Despite the different off-centered configurations, the core always stays closer to its nearest wall. The core becomes symmetric about the centerline only when the compound drop is also at the center similar to the drops under axisymmetric conditions[20–24]. It is well known that when the drop is at the centerline, there will be two circulation regions rotating in opposite directions and occupying each half of the drop. These oppositely moving circulation pushes the core towards the apex of the shell as shown by the drop *IV* in Fig. 7. A slight deviation of the drop's position from the centerline alters the flow inside the shell making one of the circulations dominant thereby resulting in an asymmetric core position as shown by the drop *III* in Fig. 7.

The concentric drop configuration used as initial condition in our simulations is rarely realized in experiments. Hence, we studied the effect of initial eccentricity of the core on the migration and deformation dynamics of the core and the compound drop (see supplementary information). In addition, we also studied the effect of the initial release height of the drop. Based on the results, we find that the initial conditions only affect their transient dynamics, while their equilibrium behavior

remains the same.

C. Core-shell interaction

From the results discussed above, we find that the core and the shell interact through the liquid between them as follows. The ambient flow conditions inside the channel deforms the compound drop by shearing its interface, and the resulting deformation induced lift force causes the compound drop to migrate. The shearing of the shell interface causes the liquid inside it to circulate, which makes the core to revolve. This revolving core, when it comes closer to the shell in each cycle, squeezes the liquid in the gap between them thereby creating a pressure buildup. Through this pressure buildup in each cycle, the core causes the compound drop to oscillate as it migrates, and also to undergo breathing motion. As the compound drop migrates towards its equilibrium position, the continuous change in its position also alters the circulation inside it due to the change in shearing rate of the shell. The changing circulation affects the revolving motion of the core which in turn affects the compound drop dynamics. Once the drop reaches its equilibrium position, the shearing force on the shell becomes steady and thus a steady circulation inside it. The nature of the rotational flow field inside the shell determines the equilibrium behavior of the core. If the strain rate tensor is dominant, we observe stable state where the core stops revolving and starts translating outwards very slowly. Limit-cycle state behavior occurs if the vorticity tensor is dominant, where the core continues to revolve in a fixed orbit. Thus, the presence of core in both states enhance the deformation of the compound drop and also affect its migration. The compound drop in turn affects the position of the core inside the shell and also its equilibrium behavior by altering the circulation. Thus, we find that the core-shell interaction affects both the core and the compound drop dynamics.

D. Parametric Study

In this section, we investigate the influence of each parameter on the core-shell interaction and their effects on the core and the compound drop dynamics. Since the transient dynamics depend strongly on the initial conditions, we only report the equilibrium behavior. We represent the oscillating behavior of the limit-cycle state cases by taking its average with error bars which represents the maximum and minimum values.

1. Effect of viscosity ratio and capillary number

The effect of viscosity ratio and capillary number on the equilibrium behavior of the compound drop and the core are shown in Fig. 8 and Fig. 9, respectively. The parameter values $\lambda = 0.2$, $K = 0.5$, and $Ca = 1$ were used while varying viscosity ratio, and $\lambda = 0.2$, $K = 0.5$, and $\mu_r = 1$ were used while studying the effect of Ca.

The deformation of the compound drop characterized by the parameter $\mathscr{D}$ are shown in Fig. 8(a) and Fig. 9(a) for varying viscosity ratio and capillary number, respectively. We observe that the deformation of the compound drop remains nearly the same as the simple drop till $\mu_r = 0.1$, and starts increasing thereafter till $\mu_r = 1$. The nearly constant deformation of the drops at low viscosities have also been experimentally observed for drops moving circular tubes[46]. As expected, similar to the simple drop, the deformation of the compound drop also increases with increasing Ca. The presence of core enhances the deformation of the compound drop, and thus it is always higher than the simple drop except at low values of Ca and μ_r, where it is nearly the same as the simple drop. The deformation of the core increases with the increase in either μ_r or Ca. Limit-cycle state behavior is observed only for low values in μ_r and Ca. Thus, we observe a transition from limit-cycle state to stable state with increase in either μ_r or Ca.

The variation of the equilibrium position of the compound drop with μ_r and Ca are shown in Fig. 8(b) and Fig. 9(b). As mentioned before, similar to the simple drop, we also observe the compound drop to move towards the center if $\mu_r < 1$ and to the wall if $\mu_r > 1$. The compound drop moves towards the center with increase in Ca due to the increase in deformation. The equilibrium position of the compound drop is always higher than the simple drop in the range of μ_r studied. Similar observations can be made with Ca but only at higher values where we observe stable state behavior. At low Ca, the equilibrium position of the simple drop is slightly higher than the compound drop due to its limit-cycle behavior as explained in section III B 2.

The variation of the eccentricity of the core as shown in Fig. 8(c), where the eccentricity in both directions increases a little till $\mu_r = 0.25$, and starts decreasing at a relatively higher rate thereafter. The eccentricity of the core (see Fig. 9(c)) in the vertical direction remains nearly constant with increase in Ca, while in the horizontal direction it decreases with increase in Ca. These trends in the eccentricity can be understood using the migration of the compound drop. When the drops are off-centered, the core occupies the backward part of the shell either at the top (see drop I in Fig.7) or at the bottom (see drop II in Fig. 7) of the shell depending upon the equilibrium position of the drop. As the centroid of the compound drop moves closer to the center, the core starts moving forward to the apex of the shell with its height ε_y (see drop III in Fig. 7) gradually decreasing till it reaches the centerline.

2. Effect of aspect ratio

Figure 10 shows the effect of aspect ratio on the equilibrium behavior of the compound drop and the core with $K = 0.5$, $Ca = 1$, and $\mu_r = 1$. The deformation of the compound drop, as shown in Fig. 10(a), increases with the drop size due to the additional deformation from the confinement effects. The deformation of the compound drop is higher than the simple drop due to the core. The deformation of the core also increases with λ but decreases slightly once the compound drop is at the center, which happens when $\lambda > 0.3$. This reduction

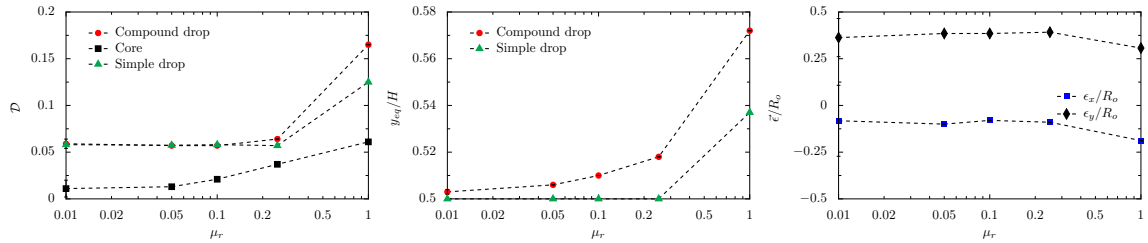

(a) (b) (c)

FIG. 8: Effect of viscosity ratio on the (a) deformation of the compound drop and the core, (b) migration of the compound drop, and (c) eccentricity of the core at equilibrium. Other parameters were kept fixed at $\lambda = 0.2$, $K = 0.5$, and $Ca = 1$.

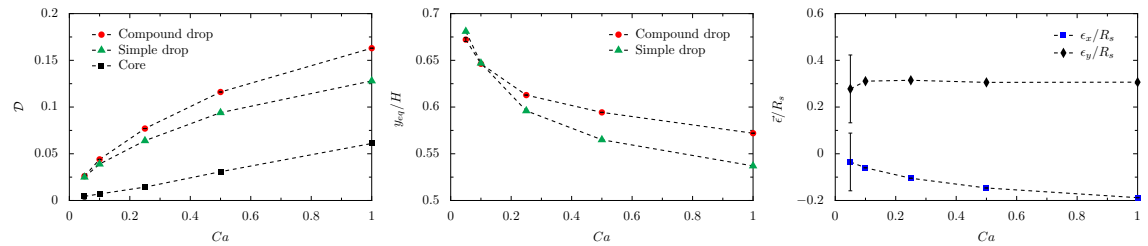

(a) (b) (c)

FIG. 9: Effect of capillary number on the (a) deformation of the compound drop and the core, (b) migration of the compound drop, and (c) eccentricity of the core at equilibrium. Other parameters were kept fixed at $\lambda = 0.2$, $K = 0.5$, and $\mu_r = 1$.

in deformation of the core is probably due to its position at the apex of the shell (see drop IV in Fig. 7), and has also been reported for compound drops moving in a circular pipe[24]. We observed only stable state behavior in the entire range studied since Ca was fixed at 1, which makes the rate of strain tensor component dominant inside the shell. At lower Ca, we expect limit-cycle state in smaller drops since they deforms less compared to large drops.

The variation of equilibrium position of the compound drop with its size is shown in Fig. 10(b). The compound drop moves towards the center with increase in size similar to the simple drop. While the simple drop reaches center when $\lambda \geq 0.3$, the compound drop reaches the center only when $\lambda > 0.3$. This slight increase in threshold size for reaching the center is due to the presence of the core, which pushes the compound drop towards the wall.

The variation of eccentricity of the core with λ is shown in Fig. 10(c). The eccentricity in the vertical direction initially increases with λ, but reaches zero when the compound drop is in the center. The eccentricity in horizontal direction initially decreases and starts increasing reaching its maximum when the compound drop is at the center. The core as shown in Fig. 7 occupies backward part of the shell at the top, and as the drop moves towards the center the core starts moving forward to the front slowly, which explains the increasing trend in eccentricity.

3. *Effect of radius ratio*

Figure 11 shows the effect of radius ratio on the equilibrium behavior of the compound drop and core with $\lambda = 0.2$, $Ca = 1$, and $\mu_r = 1$. The deformation of the compound drop as shown in Fig. 11(a), increases with core size till $K = 0.5$ and starts decreasing till $K = 0.7$, where it is nearly the same as the simple drop. At the smallest core size ($K = 0.1$) simulated, we also find that the deformation of the compound drop slightly smaller than the simple drop. Such reduction in $\mathscr{D}$ at extreme core sizes have also been observed for compound drops moving in circular pipes[24], and in shear flows[16–18,47,48]. The reduction in deformation at small core sizes occurs due to the low interaction between the core and the shell[16]. Larger cores tend to force the shell interface conform to its shape which affects the local strain inside the shell, and this reduces the deformation of the compound drop[47]. The deformation of the core, however, increases monotonically with its size due to the decrease in the capillary force. Thus, we observe a transition from limit-cycle to stable state behavior with increase in core size.

The equilibrium position of the compound drop increases with the core size as seen in Fig. 11(b), which indicates that the drop moves increasingly towards the wall. This behavior with core size confirms that the presence of core pushes the compound drop towards the wall. The equilibrium position is slightly lower than the simple drop when the core size is smallest due to its limit-cycle behavior.

The eccentricity of the core as shown in Fig. 11(c), decreases in vertical direction and increases in horizontal direc-

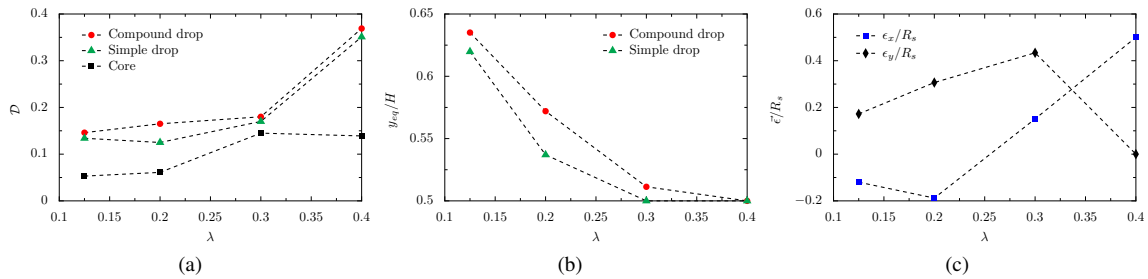

FIG. 10: Effect of aspect ratio on the (a) deformation of the compound drop and the core, (b) migration of the compound drop, and (c) eccentricity of the core at equilibrium. Other parameters were kept fixed at $K = 0.5$, $\mu_r = 1$ and $Ca = 1$.

tion with K. This decreasing trend shows that the core moves towards the center. As the core becomes larger it forces the shell to conform to its shape, which makes the centroid of the core gradually move closer to the centroid of the compound drop.

Based on the simulations, we have constructed a regime map of K versus Ca with $\lambda = 0.2$ and $\mu_r = 1$, which shows the two equilibrium core behaviors and their transition from one to the other. From Fig. 12, we observe that the transition from limit-cycle state to stable state behavior occurs with increasing either K or Ca. We also find that the threshold Ca above which the stable state is observed increases with decrease in K. This behavior is expected since smaller cores undergo less deformation compared to larger cores at a given capillary number.

IV. SUMMARY

We have investigated numerically the hydrodynamics of a compound drop suspended in a Poiseuille flow under Stokes regime. Our results show that the core and shell interact and influence each other through the liquid in the gap between them. The core starts revolving about the centroid of the compound drop initially due to the circulation inside the shell. At equilibrium, we identify two distinct equilibrium core behaviors: stable state and limit-cycle state. In the stable state the core stops revolving and starts moving outward very slowly. The core in the limit-cycle state, continues to revolve at a constant rate and in nearly a fixed orbit. By comparing with the simple drop, we find that the core in these two states enhance the deformation of the compound drop and also affects its migration. The slow outward motion of the core in the stable state pushes the compound drop slightly towards the wall, while the revolving core in the limit-cycle state makes the compound drop to oscillate in its equilibrium position. We also find that the direction of migration of the compound drop affects the eccentricity of the core.

We also conducted a parametric study to understand the influence of each parameter on the core-shell interaction. The key results are the following.

- Increasing any parameter results in the transition from limit-cycle state to stable state, which occurs due to the increased deformation of the core.
- The deformation of the compound drop is enhanced only at intermediate core sizes. At extreme sizes, the deformation of the compound drop is nearly same as the simple drop. This behavior is due to either very less interaction at small core sizes or the increased interactions at large sizes.
- The migration of the compound drop moves increasingly towards the wall with increasing core size.
- Both the core and the shell become symmetric about the centerline only when the equilibrium position of the compound drop is at the center. Even in this symmetric position, the core is still eccentric where it occupies the front of the shell.

The similarities with the results reported in the literature shows that the essential physics of the compound drops in Poiseuille flows is captured sufficiently by our 2D simulations. We believe these results provide a better understanding of the compound drops in pressure-driven flows, which can be used to identify favorable flow conditions for various applications.

V. SUPPLEMENTARY MATERIAL

The supplementary material contains equilibrium data for all the cases simulated, and plots showing the effect of initial conditions on the dynamics of the core and the compound drop.

ACKNOWLEDGMENTS

V.T.G would like to acknowledge the financial support from IIT Madras via the institute post-doctoral fellowship. **V.T.G** is grateful for insightful discussions with Mr. Akash Choudary, Mr. K.V.S Chaithanya, and Mr. Prathamesh M. Vinze. We also thank the anonymous referees for providing valuable suggestions to improve the manuscript.

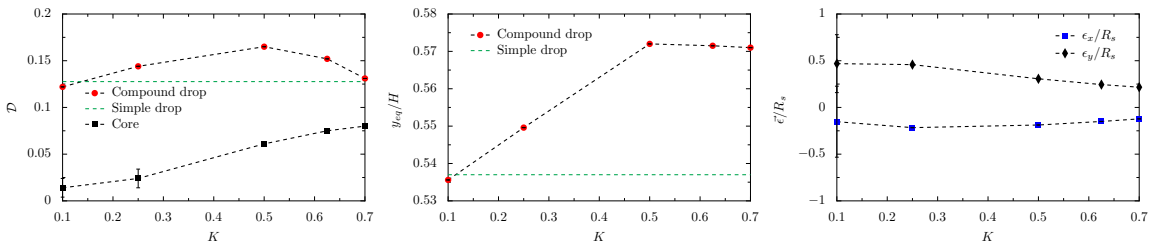

(a) (b) (c)

FIG. 11: Effect of radius ratio on the (a) deformation of the compound drop and the core, (b) migration of the compound drop, and (c) eccentricity of the core. Other parameters were kept fixed at $\lambda = 0.2$, $\mu_r = 1$ and $Ca = 1$.

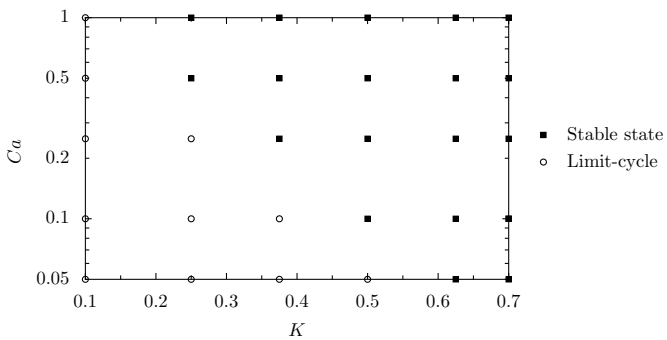

FIG. 12: Regime map showing the two equilibrium states in (K, Ca) space. Other parameters were kept fixed at $\lambda = 0.2$ and $\mu_r = 1$.

VI. DATA AVAILABILITY

The data that supports the findings of this study are available within the article and its supplementary material.

Appendix A: Derivation of the Source term S_p

In our simulations, we have used periodic boundary conditions to reduce the computational resources by limiting the size of the computational domain. The use of periodic boundary condition requires the pressure gradient (dp/dx) along the axial direction which drives the flow, to be included as a source term $\mathbf{S_P}$ in Eq. (2). This pressure gradient for plane Poiseuille flow can be expressed in terms of the velocity profile as shown below.

The velocity profile for the plane Poiseuille flow is given as,

$$U(y) = \left(\frac{1}{2\mu_c}\right)\left(\frac{dp}{dx}\right)(Hy - y^2). \tag{A1}$$

The maximum velocity U_m, which occurs at the center of the channel $(y = H/2)$ is,

$$U_m = \left(\frac{H^2}{8\mu_c}\right)\left(\frac{dp}{dx}\right). \tag{A2}$$

Rewriting the above equation in terms of pressure gradient we get the source term,

$$\mathbf{S_P} = \frac{8\mu_c U_m}{H^2}\hat{x}, \tag{A3}$$

where $\mathbf{S_p}$ is the pressure gradient.

Appendix B: Grid independence study

We perform a grid convergence test to ensure that the results are independent of grid resolution. Since we use adaptive mesh refinement, we simply vary the maximum refinement levels between 8 to 10. The size of the smallest region resolved for levels 8, 9 and 10 are 3.9×10^{-3}, 1.9×10^{-3} and 9.8×10^{-4}, respectively. The results of the test are shown in Fig. 13 for the trajectory of the compound drop and the eccentricity of the core. It can be concluded that the variation in the measured parameters between different mesh sizes is minimal, so we use a maximum refinement of 9 levels for all our simulations.

Appendix C: Validation

We verify the validity of the numerical solver used in this work with the experimental and numerical results reported in the literature[33,46] on simple drops in Poiseuille flow. First we validate the solver for drops migrating in a capillary tube[46] at different capillary numbers. This problem is simulated under Stokes regime in axisymmetric configuration, and the computational setup is a rectangular domain of size 6×1. The steady state shapes of the drop from the simulations are compared with the shapes from the experiments in Fig. 14, and we find that the solver is able to predict the shapes of the drop with sufficient accuracy.

In the second case, we verify the solver for the migration of a small drop ($\lambda = 0.125$) in a plane Poiseuille flow[33] at different viscosity ratios. We solve the full Navier-Stokes equations here (including the inertial terms) in a square computational domain of size one. Fig.15 compares the trajectory of the compound drop obtained from our simulations with the results in the literature. It shows a good agreement with the reported results from the literature.

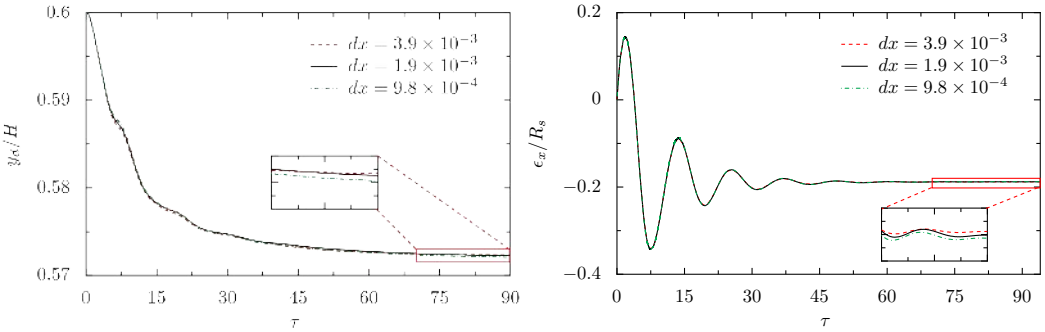

(a) (b)

FIG. 13: Effect of mesh resolution on (a) trajectory of the compound drop and (b) eccentricity of the core. The parameters used for this simulation are $\lambda = 0.2$, $K = 0.5$, $\mu_r = 1$ and $Ca = 1$.

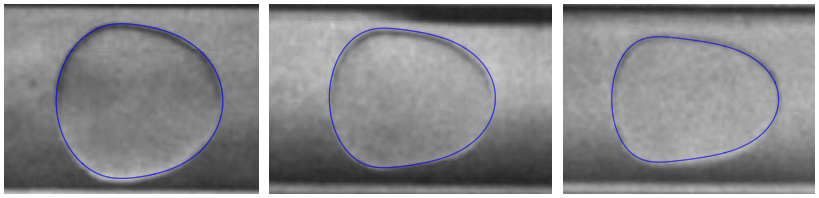

(a) (b) (c)

FIG. 14: Comparison of steady state drop shapes between the experiments[46] and the simulations (shown in blue lines) at (a) $Ca = 0.05$ (b) $Ca = 0.1$ (c) $Ca = 0.16$. Other parameters are $\mu_r = 1.05$ and $\lambda = 0.95$.

[1] M. Liu, L. Su, J. Li, S. Chen, Y. Liu, J. Li, B. Li, Y. Chen, and Z. Zhang, "Investigation of spherical and concentric mechanism of compound droplets," Matter and Radiation at Extremes **1**, 213–223 (2016).

[2] D. Liu, H. Zhang, F. Fontana, J. T. Hirvonen, and H. A. Santos, "Microfluidic-assisted fabrication of carriers for controlled drug delivery," Lab Chip **17**, 1856–1883 (2017).

[3] W. Li, L. Zhang, X. Ge, B. Xu, W. Zhang, L. Qu, C.-H. Choi, J. Xu, A. Zhang, H. Lee, and D. A. Weitz, "Microfluidic fabrication of microparticles for biomedical applications," Chem. Soc. Rev. **47**, 5646–5683 (2018).

[4] G. Muschiolik and E. Dickinson, "Double emulsions relevant to food systems: Preparation, stability, and applications," Comprehensive Reviews in Food Science and Food Safety **16**, 532–555 (2017).

[5] A. G. Håti, N. B. Arnfinnsdottir, C. Østevold, M. Sletmoen, G. Etienne, E. Amstad, and B. T. Stokke, "Microarrays for the study of compartmentalized microorganisms in alginate microbeads and (W/O/W) double emulsions," RSC Advances **6**, 114830–114842 (2016).

[6] T. Alkayyali, T. Cameron, B. Haltli, R. G. Kerr, and A. Ahmadi, "Microfluidic and cross-linking methods for encapsulation of living cells and bacteria - A review," Analytica Chimica Acta **1053**, 1–21 (2019).

[7] R. Johnson, "Fluid Mechanics of Compound Multiphase Drops and Bubbles," Annual Review of Fluid Mechanics **17**, 298–320 (1985).

[8] S. S. Sadhal and H. N. Oguz, "Stokes flow past compound multiphase drops: The case of completely engulfed drops/bubbles," Journal of fluid Mechanics **160**, 511–529 (1985).

[9] I. Bazhlekov, P. J. Shopov, and Z. D. Zapryanov, "Unsteady motion of a type-A compound multiphase at moderate Reynolds numbers," Journal of Colloid And Interface Science , 1–12 (1995).

[10] S. Homma, M. Yokotsuka, T. Tanaka, K. Moriguchi, J. Koga, and G. Tryggvason, "Numerical simulation of an axisymmetric compound droplet by three-fluid front-tracking method," Fluid Dynamics and Materials Processing **7**, 231–240 (2011).

[11] L. L. G. Stone H.A., "Breakup of concentric double emulsions droplets in linear flows," Journal of Fluid Mechanics **211**, 123–156 (1990).

[12] J. Wang, X. Wang, M. Tai, and J. Guan, "Oriented shift and inverse of the daughter droplet due to the asymmetry of grand-daughter droplets of multiple emulsions in a symmetric flow field," Applied Physics Letters **108** (2016).

[13] J. Wang, S. Xu, Y. Huang, and J. Guan, "Mechanical mechanisms of the directional shift and inverse of the eccentric compound droplet," Physics of Fluids **30** (2018).

[14] K. A. Smith, J. M. Ottino, and M. O. De La Cruz, "Encapsulated drop breakup in shear flow," Physical Review Letters **93**, 1–4 (2004).

[15] X. Qu and Y. Wang, "Dynamics of concentric and eccentric compound droplets suspended in extensional flows," Physics of Fluids **24** (2012), 10.1063/1.4770294.

[16] H. Hua, J. Shin, and J. Kim, "Dynamics of a compound droplet in shear flow," International Journal of Heat and Fluid Flow **50**, 63–71 (2014).

[17] Y. Chen, X. Liu, C. Zhang, and Y. Zhao, "Enhancing and suppressing effects of an inner droplet on deformation of a double emulsion droplet under shear," Lab on a Chip **15**, 1255–1261 (2015).

[18] Y. Chen, X. Liu, and Y. Zhao, "Deformation dynamics of double emulsion droplet under shear," Applied Physics Letters **106** (2015).

[19] T. V. Vu, T. V. Vu, and D. T. Bui, "Numerical study of deformation and breakup of a multi-core compound droplet in simple shear flow," International Journal of Heat and Mass Transfer **131**, 1083–1094 (2019).

[20] C. Zhou, P. Yue, and J. J. Feng, "Deformation of a compound drop through a contraction in a pressure-driven pipe flow," International Journal of Multiphase Flow **34**, 102–109 (2008).

[21] Y. Song, J. Xu, and Y. Yang, "Stokes flow past a compound drop in a circular tube," Physics of Fluids **22**, 1–19 (2010).

[22] J. Tao, X. Song, J. Liu, and J. Wang, "Microfluidic rheology of the multiple-emulsion globule transiting in a contraction tube through a boundary element method," Chemical Engineering Science **97**, 328–336 (2013).

[23] M. P. Borthakur, G. Biswas, and D. Bandyopadhyay, "Dynamics of deformation and pinch-off of a migrating compound droplet in a tube," Physical Review E **97**, 1–9 (2018).

[24] Z. Che, Y. F. Yap, and T. Wang, "Flow structure of compound droplets moving in microchannels," Physics of Fluids **30** (2018).

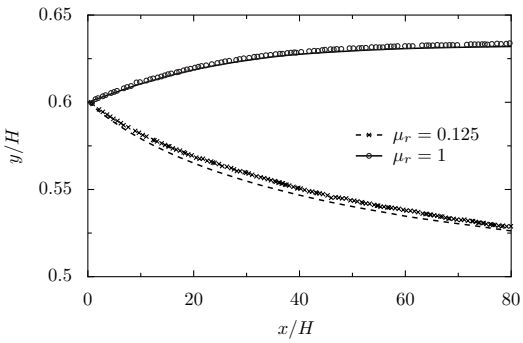

(a)

FIG. 15: Trajectory of the drop at $Re(= U_m H/\nu_c) = 1,\ Ca = 0.25,\ \lambda = 0.125$. The lines represent current simulation and the markers represent the simulation data from[33].

[25] S. Guido and V. Preziosi, "Droplet deformation under confined poiseuille flow," Advances in Colloid and Interface Science **161**, 89 – 101 (2010), physico-chemical and flow behaviour of droplet based systems.

[26] P. C. Chan and L. G. Leal, "The motion of a deformable drop in a second-order fluid," Journal of Fluid Mechanics **92**, 131–170 (1979).

[27] C. Yu, L. Wu, L. Li, and M. Liu, "Experimental study of double emulsion formation behaviors in a one-step axisymmetric flow-focusing device," Experimental Thermal and Fluid Science **103**, 18–28 (2019).

[28] J. Brackbill, D. Kothe, and C. Zemach, "A continuum method for modeling surface tension," Journal of Computational Physics **100**, 335 – 354 (1992).

[29] S. Popinet, "Gerris: a tree-based adaptive solver for the incompressible euler equations in complex geometries," Journal of Computational Physics **190**, 572 – 600 (2003).

[30] S. Popinet, "An accurate adaptive solver for surface-tension-driven interfacial flows," Journal of Computational Physics **228**, 5838 – 5866 (2009).

[31] M. M. Francois, S. J. Cummins, E. D. Dendy, D. B. Kothe, J. M. Sicilian, and M. W. Williams, "A balanced-force algorithm for continuous and sharp interfacial surface tension models within a volume tracking framework," Journal of Computational Physics **213**, 141 – 173 (2006).

[32] S. Afkhami and M. Bussmann, "Height functions for applying contact angles to 2d vof simulations," International Journal for Numerical Methods in Fluids **57**, 453–472 (2008).

[33] S. Mortazavi and G. Tryggvason, "A numerical study of the motion of drops in Poiseuille flow. Part 1. Lateral migration of one drop," Journal of Fluid Mechanics **411**, 325–350 (2000).

[34] C. A. Stan, L. Guglielmini, A. K. Ellerbee, D. Caviezel, H. A. Stone, and G. M. Whitesides, "Sheathless hydrodynamic positioning of buoyant drops and bubbles inside microchannels," Physical Review E - Statistical, Nonlinear, and Soft Matter Physics **84**, 1–19 (2011).

[35] H. Lan and D. B. Khismatullin, "A numerical study of the lateral migration and deformation of drops and leukocytes in a rectangular microchannel," International Journal of Multiphase Flow **47**, 73–84 (2012).

[36] G. I. Taylor, "The formation of emulsions in definable fields of flow," Proceedings of the Royal Society of London. Series A, Containing Papers of a Mathematical and Physical Character **146**, 501–523 (1934).

[37] S. Kim and S. Dabiri, "Transient dynamics of eccentric double emulsion droplets in a simple shear flow," Physical Review Fluids **2**, 1–17 (2017).

[38] "Reactions in double emulsions by flow-controlled coalescence of encapsulated drops," Lab on a Chip **11**, 2312–2315 (2011).

[39] M. D. Graham, *Microhydrodynamics, Brownian Motion, and Complex Fluids*, Cambridge Texts in Applied Mathematics (Cambridge University Press, 2018).

[40] Y. N. Young, J. Bławzdziewicz, V. Cristini, and R. H. Goodman, "Hysteretic and chaotic dynamics of viscous drops in creeping flows with rotation," Journal of Fluid Mechanics **607**, 209–234 (2008).

[41] J. Blawzdziewicz, R. H. Goodman, N. Khurana, E. Wajnryb, and Y. N. Young, "Nonlinear hydrodynamic phenomena in Stokes flow regime," Physica D: Nonlinear Phenomena **239**, 1214–1224 (2010).

[42] S. C. Hur, N. K. Henderson-Maclennan, E. R. McCabe, and D. Di Carlo, "Deformability-based cell classification and enrichment using inertial microfluidics," Lab on a Chip **11**, 912–920 (2011).

[43] B. V. Hokmabad, K. A. Baldwin, C. Krüger, C. Bahr, and C. C. Maass, "Topological Stabilization and Dynamics of Self-propelling Nematic Shells," Physical Review Letters **123**, 178003 (2018), arXiv:1810.07223.

[44] S. Okushima, T. Nisisako, T. Torii, and T. Higuchi, "Controlled production of monodisperse double emulsions by two-step droplet breakup in microfluidic devices," Langmuir **20**, 9905–9908 (2004).

[45] E. W. Kemna, R. M. Schoeman, F. Wolbers, I. Vermes, D. A. Weitz, and A. Van Den Berg, "High-yield cell ordering and deterministic cell-in-droplet encapsulation using Dean flow in a curved microchannel," Lab on a Chip **12**, 2881–2887 (2012).

[46] W. L. Olbricht and D. M. Kung, "The deformation and breakup of liquid drops in low reynolds number flow through a capillary," Physics of Fluids A: Fluid Dynamics **4**, 1347–1354 (1992).

[47] S. M. Hosseini and J. J. Feng, "How malaria parasites reduce the deformability of infected red blood cells," Biophysical Journal **103**, 1–10 (2012).

[48] Z. Y. Luo, L. He, and B. F. Bai, "Deformation of spherical compound capsules in simple shear flow," Journal of Fluid Mechanics **775**, 77–104 (2015).